X-ray grating interferometer for imaging at a second-generation synchrotron radiation source

Julia Herzen[a,b], Felix Beckmann[a], Tilman Donath[c,d], Malte Ogurreck[a], Christian David[d], Franz Pfeiffer[b], Jürgen Mohr[e], Elena Reznikova[e], Stefan Riekehr[a], Astrid Haibel[a], Georg Schulz[f], Bert Müller[f], and Andreas Schreyer[a]

[a]GKSS Research Centre, Geesthacht, Germany;
[b]Technische Universität München, Munich, Germany;
[c]Dectris AG, Baden, Switzerland;
[d]Paul Scherrer Institut, Villigen PSI, Switzerland;
[e]Karlsruhe Institute of Technology, Karlsruhe, Germany;
[f]Biomaterials Science Center, University of Basel, Switzerland

ABSTRACT

X-ray phase-contrast radiography and tomography enables to increase contrast for weakly absorbing materials. Recently, x-ray grating interferometers were developed which extend the possibility of phase-contrast imaging from highly brilliant radiation sources like third-generation synchrotron even to non-coherent sources. Here, we present a setup of an x-ray grating interferometer designed and installed at low-coherence wiggler source at the GKSS beamline W2 (HARWI II) operated at the second-generation synchrotron storage ring DORIS at the Deutsches Elektronen-Synchrotron (DESY, Hamburg, Germany). The beamline is dedicated to imaging in materials science. Equipped with the grating interferometer, it is the first synchrotron radiation beamline with a three-grating setup combining the advantages of phase-contrast imaging with monochromatic radiation with very high flux and a sufficiently large field of view for centimeter sized objects. Examples of radiography on laser-welded aluminum and magnesium joints are presented to demonstrate the high potential of the new grating-based setup in the field of materials science. In addition, the results of an off-axis phase-contrast tomography of a human urethra with 15 mm in diameter are presented showing internal structures, which cannot be resolved by the conventional tomography in absorption mode.

Keywords: Phase contrast, synchrotron radiation, grating interferometer, materials science, laser-beam weld, soft-tissue imaging

1. INTRODUCTION

In the well established conventional x-ray imaging method in absorption mode good contrast between different weakly absorbing materials inside an object is hard to achieve. To image materials consisting of weakly absorbing elements, especially organic materials, different contrast media or staining procedures are often required. However, such treatments are time consuming, difficult, and in some cases may not be possible or cause structural changes. Detecting the changes in the x-ray wave front caused by the object, in so-called *phase-contrast imaging*, the contrast for weakly absorbing materials can be significantly enhanced using the phase shift introduced to the x-ray wave by the object as a contrast mechanism in the same energy range.

In the last decades, different methods were developed to use the phase shift as contrast mechanism.[1–5] For a long time, these methods have been practically limited to highly brilliant radiation as it is available at e. g., third generation synchrotron radiation sources. Recently, the development of grating interferometers extend x-ray phase-contrast imaging even to conventional x-ray tube sources.[6–9] Therefore, grating-based x-ray phase-contrast imaging became feasible also at the second generation synchrotron radiation sources. These radiation

---

sources provide several orders of magnitude more flux than conventional x-ray tubes, but a much lower brilliance than third generation sources (ESRF/France, PETRA III/Germany), and monochromatic radiation for characterizing centimeter sized objects.

In this paper we describe a three-grating interferometer setup that was built in cooperation with Paul Scherrer Institut (Switzerland), TU München and Karlsruhe Institute of Technology (KIT) (Germany), and installed at the beamline W2 (HARWI II) operated by GKSS Research Centre Geesthacht at the storage ring DORIS (DESY, Germany). This is the first grating interferometer setup at a second generation synchrotron storage ring utilizing three gratings and serves as proof of principle of this geometry using a large and distant source point. A radiography on aluminum and magnesium joints produced by laser welding, and a tomography of an unstained human male urethra fixed in PBS solution are presented to demonstrate the high performance of the new setup.

2. INSTRUMENTS AND METHODS

2.1 The beamline W2

The wiggler beamline W2 has been equipped with a grating interferometer. It is situated at the storage ring DORIS III and operated by the GKSS Research Centre Geesthacht (GKSS) in cooperation with DESY since 2006 as a high energy materials science beamline. The technical details of the beamline have been published by Beckmann et al.[10, 11] and in the book by Reimers, Pyzalla, Schreyer, and Clemens.[12]

Two monochromator setups, one with horizontal and one with vertical beam reflection, are installed at W2. The horizontal monochromator is used for diffraction applications. The vertical one provides a wide beam up to 70 (horizontal) x 8 (vertical) mm^2 making it particularly suitable for tomographic imaging. Different pairs of crystals are in Laue-Laue and Laue-Bragg geometry to vary the photon energy.[13, 14] The monochromator concept of the beamline W2 is presented in detail by Beckmann et al.[15]

As the wiggler beamline W2 operates at the second-generation storage ring DORIS III, its source divergence is much larger compared to that of newer third-generation synchrotron radiation sources like ESRF, SPRING 8, and PETRA III with undulator sources. This fact, and the millimeter-sized source point in the wiggler, have two important consequences: 1.) It makes the beamline extremely interesting for applications on centimeter-sized objects, and 2.) it leads to a very low spatial coherence in the x-ray beam, that makes direct phase-contrast imaging practically impossible. The beamline can be treated like an extended incoherent x-ray source (like a conventional x-ray tube) and phase-contrast methods designed for this type of sources can be considered for it. The phase-contrast method using a three-grating interferometer has been used with incoherent sources (x-ray tubes and neutrons[7, 9, 16, 17]) and was redesigned for the beamline W2, meaning that the grating geometries had to be adjusted to the beamline. Additionally, due to the large source point a compromise between a high sensitivity of the interferometer at high intergrating distances and the image blur by the beam divergence at larger sample-to-detector distances had to be found.

2.2 The X-ray detector

The x-ray detector consisted of a luminescence screen, a commercial lens, and a CCD camera. As a luminescence screen a CdWO$_4$ crystal 587 μm thick with the front side (the side facing the x-rays) covered by a black lacquer was used.[18] A commercial Nikkor 50 mm f1.8 lens (Nikon, Japan) operated in retro-focus position (facing the luminescence screen with the side, that is normally facing the CCD chip) with a focal length of 50 mm was used. The amount of light and the resolution can be controlled by the aperture inside the lens. A PLO9000 CCD camera (Finger Lakes Instrumentations, USA) with an active area of 3056x3056 pixels with a pixel size of 12 μm was used. The CCD camera uses an internal iris shutter to protect the CCD from illumination during the read out. The CCD is cooled down to -15° C by an internal Peltier element during the operation. In full frame operation the CCD digitalizes with 16 bit at 10 MHz (true dynamic range ≈ 13 bit). The typical exposure times were between 0.3 and 10.0 seconds per image with a full frame read-out time of 1 second. The quantum

efficiency of the CCD chip of the camera and the emitted intensity of the luminescence screen have both a peak in the visible light regime at a wavelength of ≈ 500 nm.

2.3 Grating-based imaging

The principle of the self-imaging effect using the x-ray grating interferometer has been explained in detail by many authors.[6,8,19,20] The images were taken similar to the procedure described by these authors, thus, this procedure will be very briefly described here.
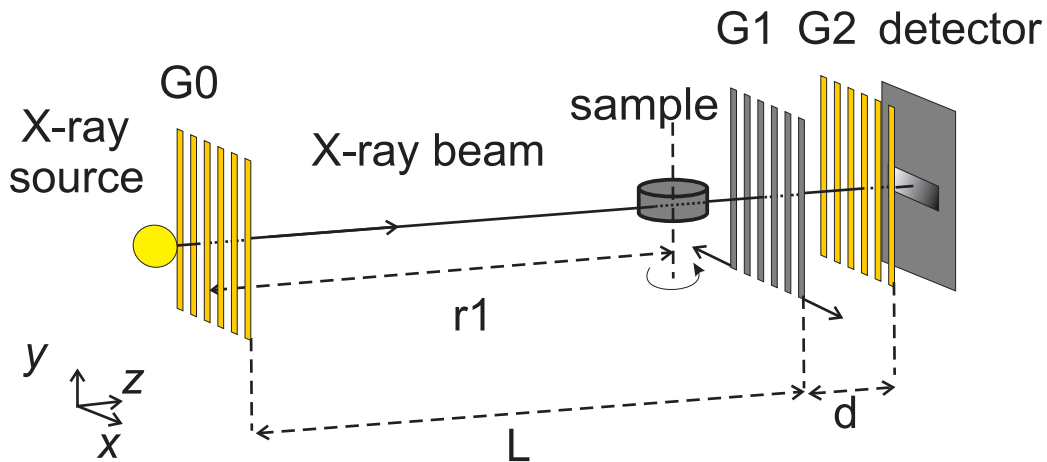

Figure 1. Schematic of a Talbot grating interferometer working with low-brilliance radiation sources. It consists of three gratings, the absorbing source grating G_0, the phase grating G_1, and the absorbing analyzer grating G_2.

Figure 1 shows a schematic of a Talbot grating interferometer working with low-brilliance radiation sources and consisting of three gratings. The source gold grating G_0 with the period p_0 divides a large source into many small mutually incoherent line sources with higher lateral coherence of each individual line source. The measurements presented here were performed at a wiggler source with a source spot size of 1.7 mm in horizontal direction.

The partially coherent beam illuminates the central phase grating G_1 with the period p_1 that is designed to introduce a phase shift of π on the incoming wave field. This phase shift creates an interference pattern of period p_2 in certain discrete distances (Talbot distances) behind the G_1. The grating interferometer measures the beam refraction caused by an object. This refraction shifts laterally the interference pattern. By detecting this lateral shift the object's differential phase shift can be measured. Since the fringes cannot be resolved directly with a conventional x-ray detector, a so-called *phase-stepping scan* is performed by shifting one grating perpendicular to the beam and taking images at each position. Typically, the phase-stepping scan is performed over one period of the interference pattern taking at least 4 images. In our case the G_1 is shifted relatively to the other two gratings. The intensity oscillation during this phase-stepping scan is recorded for each pixel.

The periodical oscillation can be described by a cosine function and by determining the mean value, the amplitude and the phase shift of the intensity oscillation in each detector pixel three signals can be extracted: the conventional attenuation, the differential phase signal, and the dark-field signal.[8,21]

The tomographic reconstruction is performed using the standard backprojection algorithm with the Hamming filter for the attenuation and the dark-field projections. For the differential phase projections an imaginary Hilbert filter is used during the reconstruction.[7]

2.4 Experimental implementation of the interferometer

2.4.1 Interferometer geometries

The x-ray grating interferometer designed for the low-coherence beamline W2 consists of three gratings: an absorbing source grating G_0 (Au), a beam-splitter grating G_1 (Si, phase shift of π), and an absorbing analyzer grating G_2 (Au). The principle of such an interferometer is explained in the previous section.

The periods and the depths of the gratings for the setup at the beamline W2 are listed in Table 1. To switch between the different fractional Talbot orders the photon energy has to be changed while the inter-grating distances are kept fixed. So, we should derive the *Talbot wave lengths* instead of the distances for our grating interferometer. The interferometer is usable in the energy range 22-30 keV corresponding to 7th (22 keV), 6th (24 keV), and 5th (30 keV) Talbot order.

Table 1. Grating properties

The list of the grating geometries designed for the beamline W2. The two gold gratings G_0 and G_2 are usable in the energy range below the given energy (absorption of 90 % at the given energy) and the two phase gratings G_1 are optimized for the design energies. Above the design energy of the gold gratings the interference pattern visibility decreases, as the grating absorption becomes insufficient. The use of the phase grating G_1 at its design energy increases the visibility, since then the phase shift induced by the grating is almost π. The source grating G_0 consists of two areas: one with a duty cycle 0.7 to increase visibility and the other with 0.5 to have more photon flux.

Grating	design energy E_{ph} $[keV]$	period p $[\mu m]$	height h $[\mu m]$	duty cycle $DC \pm std$
phase grating G_1#1	27.3	4.33	35	0.42 ± 0.02
phase grating G_1#2	32.7	4.33	42	0.54 ± 0.04
source grating G_0	30	22.29	45-50	0.7/0.5
analyser grating G_2	25	2.4	30.8	0.5

2.5 Mechanical components

The grating-based imaging system consists of an x-ray detector, an air beared high precision rotation axis and the motorized grating holder with 6 motors for alignment and 1 piezo (HERA 100, PI, Germany) for stepping the phase grating G_1. The source grating is placed on the diffractometer in front of the imaging setup providing many degrees of freedom for adjusting the G_0 in respect to the other two gratings.

The absorbing gold grating G_0 and the phase grating G_1 were fabricated by C. Grünzweig and C. David at the Paul Scherrer Institut (Villigen/PSI) in Switzerland. Both these gratings were produced on 4 inch silicon wafers in a fabrication process involving photolithography, deep etching into silicon and for the absorption grating G_0 electroplating of gold. The fabrication process of these two gratings is described in detail by David *et al.*[22] The analyzer gold grating G_2 is produced by E. Reznikova and J. Mohr from Karlsruhe Institute of Technology (KIT), Karlsruhe, Germany. It is more critical, as the same height is required as for the source grating G_0 but the period is one order of magnitude smaller.

2.6 Phase-contrast radiography of laser-welded materials

The GKSS Research Centre runs an Nd:YAG laser with a 400 μm fiber, a focal length of 200 mm and a laser power of 3 kW. The in-house laser welds are produced using this laser. Helium is used as shielding gas during the welding process and the angle between the skin and the laser beam can be altered. However, some amount of small pores (due to for example entrapment of oxygen) may occur within the molten metal. No artificial attempt was made to produce porous weld metal. By varying the welding speed and the welding angle the properties of the produced laser weld can be influenced. Also the porosity within the weld strongly depends on the process

parameters as well as alloy composition.

Butt-joints welded by the laser-welding method described above were imaged using the phase-contrast radiography (PCR). Figure 2 shows the two specimens used for this study: (a) the magnesium alloy joint (2.5 mm thick; material AZ31, 3% aluminum, 1% zinc, density: 1.8 g/cm^3) and (b) the aluminum alloy joint (2.8 mm thick; material: AA6156, 95-98% aluminum, 1% magnesium, 1% copper, density: 2.7 g/cm^3). From both samples, small specimens were cut out in the marked region and glued to a sample holder, which was placed on the CT-rotation axis of the grating-based imaging setup. To simplify the measurement, a small part of the sample was cut out from the welded region. But also the whole joint could be put into the beam without destroying it.
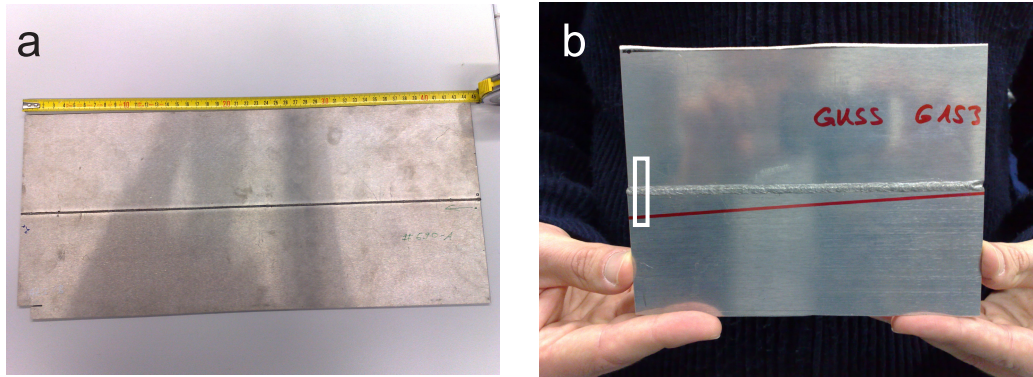

Figure 2. Picture of laser-welded butt-joints imaged using grating-based phase-contrast radiography (PCR). (a) magnesium alloy joint (2.5 mm thick; material AZ31, 3% aluminium, 1% zinc, density: 1.8 g/cm^3) and (b) aluminium alloy joint (2.8 mm thick; material: AA6156, 95-98% aluminum, 1% magnesium, 1% copper, density: 2.7 g/cm^3). From both samples small specimens were cut out in the marked regions and glued to a sample holder.

As laser-beam welding melts the basic material in the region of the weld, not only the characteristics of the alloys are changed (strength and flexibility) but also precipitations of different compound materials present in the alloy can occur and porosity can be introduced by e.g., entrapment of oxygen. The welding process can be optimized by changing the alloy composition or welding parameters like laser-beam speed and incident angle. In industrial laser-beam welding the welds are checked directly after welding using x-ray radiography with an x-ray tube and a detector.

For both specimens the projections were recorded using the grating interferometer in the 5th Talbot order at 30 keV. The beam-splitter grating G_1 #1 was used for the measurements. To obtain one projection a phase-stepping scan with 8 phase steps over two periods of the grating G_2 was performed with the specimen in the beam and without the specimen, to obtain flat field correction images (exposure time: 0.5 s per image). From the intensity changes during the phase-stepping scan three different contrast projections were calculated by means of a Fast Fourier Transform (FFT) as explained in Section 2.3 using Matlab.

2.7 Phase-contrast tomography of a human male urethra

The human male urethra ($\approx$ 15 mm diameter) embedded in a PBS solution was scanned in a plastic container in a water bath using the new grating-based setup at the beamline W2.

The specimen was embedded in a PBS solution in a polyethylene Eppendorf tube of 15 mm outer diameter. The PBS solution was degased for several hours under a low-pressure cap to avoid gas bubble formation produced by radiation damage during the scan. The Eppendorf tube with the specimen was glued to a sample holder and mounted on the CT-rotation axis hanging from above into a 25 mm thick water container filled with demineralized water. The water serves as background for the measurement to match the complex refractive

index of the specimen to that of the background to avoid phase jumps at the edges of the sample container in the phase-contrast signal.

An off-axis tomography scan with 1440 projections over 360 degrees was recorded with 8 phase-steps over two periods of the grating G_2 for each projection. Off-axis means, that the rotation axis was shifted slightly to the side and a 360 degrees scan was performed, as with a 180 degrees rotation the sample would not fit into the field of view. The phase grating was stepped during the phase-stepping scan. The exposure time was in the range of 3 seconds per image, changing during the scan to correct for the decreasing ring current of DORIS. The images were taken with a binning factor of 2. After every eighth projection a reference projection was recorded by moving the sample vertically out of the water tank. The reference projections were used to correct for beam instabilities. The effective pixel size was determined by an automated focussing procedure to be 12 μm, and the spatial resolution 37 μm at 10 % of the MTF curve (limited by the source size and the sample-to-detector distance).

Before the reconstruction the second half of the 360 degrees scan (720 projections) the sign of the projections had to be flipped and the projections had to be combined with the first half to a 180 degrees scan containing the whole sample in one projection.

The reconstruction was performed using the filtered back projection algorithm described above. The reconstructed slices were stored as floating point data and windowed to the given gray values before image export. To obtain absolute values of measured data, the reconstructed values had to be corrected for the reduced sensitivity of the grating interferometer. The recorded phase projections were renormalized by multiplication with the factor $(r_1/L)^{-1}$ prior to reconstruction, where r_1 represents the specimen distance from the source grating G_2 and L the distance between the G_0 and the phase grating G_1 (compare Fig. 1).

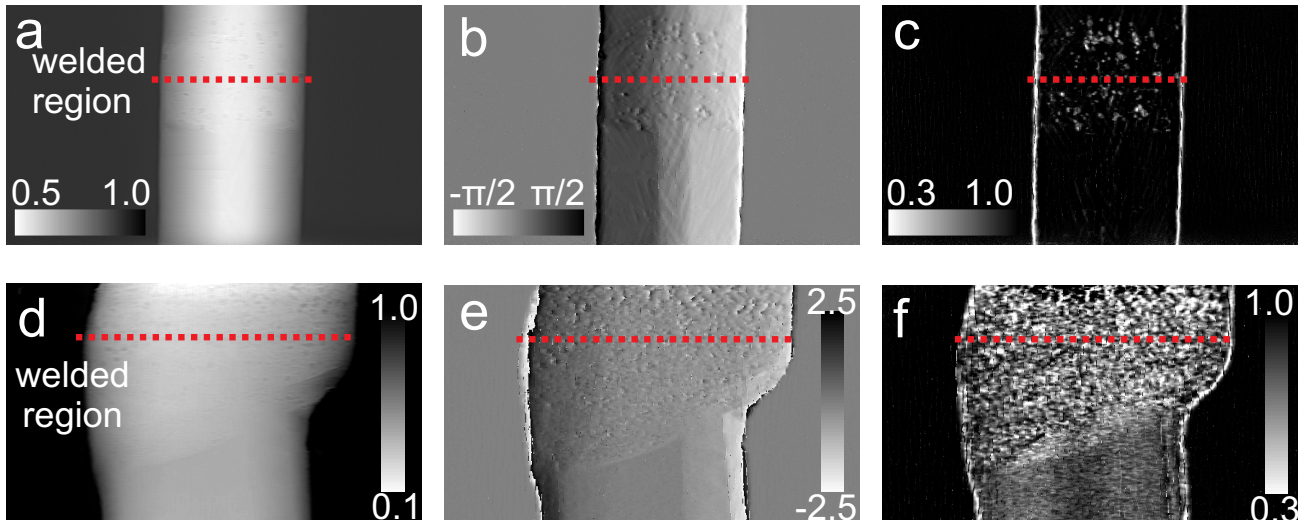# 3. RESULTS AND DISCUSSIONS

3.1 PCR of laser-welded materials

Figure 3. (a)-(c) Projections of a magnesium-alloy laser weld (material: AZ31; 30 keV, 5th Talbot order, field of view: 4x6 mm^2). (a) The transmission (b) the differential phase contrast and (c) the dark-field contrast of the same region of the sample. The dark-field and the differential phase-contrast signals show better contrast in the welded region, while the transmission shows only poor contrast for inner structures. (d)-(f) Projections of an aluminum-alloy laser weld (material: AA6156; 30 keV, 5th Talbot order, field of view: 4x6 mm^2). (d) X-ray transmission, (e) the differential phase contrast, and (f) the dark-field contrast. The differential phase contrast and the dark-field signals increase in the welded region, while the transmission is almost the same.

Figure 3 shows the results of the PCR measurement of the magnesium-alloy (a)-(c) and aluminum-alloy (d)-(f) butt-joints. Figures 3(a) and (d) show the transmission pictures of both specimens similar to that, one would obtain using a conventional absorption-contrast mode. In the welded region marked in the Figure, only weak contrast of inner structure of the weld can be seen (here: porosity and precipitations), while the base material (bottom part of the specimens) absorbs homogeneously. Although the specimens were measured in air, this setup should produce enough contrast due to the large density difference of air and magnesium or aluminum ($\rho_{air} = 0.0012$ g/cm^3 and $\rho_{Mg} = 1.74$ g/cm^3, $\rho_{Al} = 2.7$ g/cm^3). But in the projections one can hardly define the position and the size of the pores and precipitates inside the welded regions. The problem can be solved by performing a whole tomography scan of the specimens, rotating it over 180 degrees and recording projections from many different angles. The reconstructions would show a high density and spatial resolution, thus, the localization of porosity and precipitates would be easily possible. But as already mentioned a whole tomography is too time-consuming and destructive as the sample has to be downsized, since the spatial resolution depends on the total sample size. Thus it would not match the real conditions of the quality assurance procedure during the welding process in industrial applications.

Looking at the other two signals provided by the grating interferometer, one can clearly distinguish between the welded region and the basic material (see Figure 3(b) and (e) for differential phase contrast and (c) and (f) for dark-field contrast. Both signals rise at each edge inside and outside the specimens, so the borders of the samples produce a very high signal in both contrasts. In the differential phase contrast 'phase-wrapping' can be seen at the edges of the sample. This effect occurs when the amount of phase-shift exceeds several times π due to the large difference between the complex refractive index decrements δ of the air and the material. Phase-wrapping would produce strong artifacts in tomographic reconstructions and should be removed by an adequate algorithm prior to reconstructions, but it is not important for our purpose, as we were only interested in radiographic projections. Nevertheless, using the differential phase contrast the welded region of both specimens can be clearly localized.

The dark-field signal clearly shows the changes in the welded regions of the specimens compared to the basic material. Since this signal is similar to the small-angle scattering signal, the structure of the material was changed by laser-beam welding in such a way, that small-angle scattering signal rises. As the interferometer is sensitive only to structures in the range of few μm, such structures must appear in the weld. The basic material of the magnesium sample seems not to produce a dark-field signal, thus, only the porosity inside the weld can be seen. In the aluminum specimen the basic material also produces dark-field signals, but it increases in the welded region, as precipitations appear after welding increasing the dark-field signal.

3.2 PC-CT of human male urethra

In Figure 4 the tomographic reconstruction of the phase-contrast signal of the human male urethra is shown. The top part shows an axial slice, and the bottom part shows the cut along the red line. The phase-contrast reconstruction provides a detailed information about the inner structure of the specimen. In the urethra tissue as well as in the tissue around the lumen (the inner opening in the middle of the urethra), different structures can be distinguished. The reconstructions of the dark-field signal are not shown here, as similarly to the absorption contrast it does not show any information about the specimen.

The results of the phase-contrast tomography scan of a human male urethra demonstrate the high contrast for such weakly absorbing materials in fluid environment. The off-axis tomography do not produce any artifacts in the reconstructions. This approach shows, that the field of view can be significantly enlarged to analyze several centimeters large objects without compromising on the image quality. The fact that no information of these specimens could be gained from the absorption and the dark-field contrasts, points out the importance of the newly available phase-contrast method at the beamline W2.
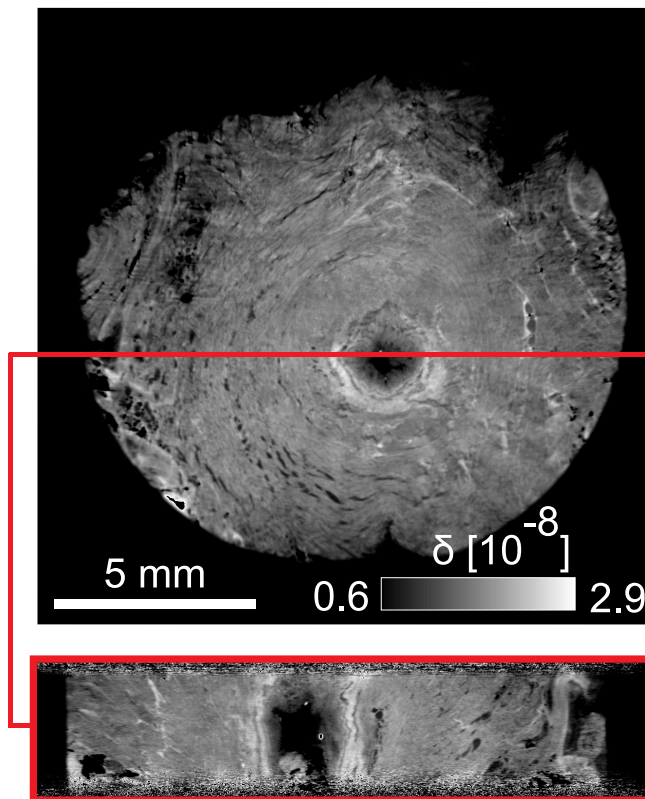
Figure 4. Tomographic reconstruction of a human male urethra. (top) axial slice through the urethra, measured in water bath at the 6th Talbot order and 24 keV, binning factor 2, spatial resolution 37 μm.

4. CONCLUSIONS

The special assets of the PCR are its ability to provide three different contrast simultaneously allowing to judge the quality of the weld from simple projections by combination of the information from the signals. Using the synchrotron radiation beamline W2 very short exposure times (due to high flux) and high spatial resolution at large field of view sizes compared to other synchrotron beamlines (now: 6 mm × 30 mm; in future: 6 mm × 60 mm) can be achieved in PCR projections. As a possible future task, the PCR at the beamline W2 can be expanded to imaging other welding processes like Friction Stir Welding (FSW). It can even be used for in-situ imaging to visualize the changes in the welded region on the fly in combination with the in-situ welding machine FlexiStir.[23, 24]

It has been shown that using the grating-based imaging method soft tissue can be measured without complicated and time-consuming sample preparation procedures. Even imaging of unique and very valuable samples can be done by this method without destroying or changing its structure. A reconstruction of an off-axis phase-contrast tomography using the Talbot grating interferometer is demonstrated to yield artifact-free images.

These measurements clearly demonstrate the power of the new grating-based setup to image centimeter-sized soft-tissue samples in fluid environment. It benefits from the ability to choose the optimum photon energy for each specimen (from the range of 22-30 keV) and from the high photon flux, keeping the exposure times short. In addition, it makes quantitative measurements easier, as the reconstructions do not suffer from polychromatic artifacts.

ACKNOWLEDGMENTS

REFERENCES

1. U. Bonse and M. Hart, "An X-ray interferometer," *Appl. Phys. Lett.* **6**, pp. 155–156, 1965.

2. F. Beckmann, U. Bonse, F. Busch, and O. Günnewig, "X-ray microtomography (μCT) using phase contrast for the investigation of organic matter," *Journal of Computer Assisted Tomography* **21(4)**, pp. 539–553, 1997.

3. P. Cloetens, W. Ludwig, J. Baruchel, D. van Dyck, J. van Landuyt, J. P. Guigay, and M. Schlenker, "Holotomography: Quantitative phase tomography with micrometer resolution using hard synchrotron radiation x rays," *Applied Physics Letters* **75**, pp. 2912–2914, 1999.

4. A. Momose, "Demonstration of phase-contrast X-ray computed tomography using an X-ray interferometer," *Nuclear Instruments and Methods A* **352**, pp. 622–628, 1995.

5. A. Momose, "Recent advances in X-ray phase imaging," *Japanese Journal of Applied Physics* **44**, pp. 6355–6367, 2005.

6. F. Pfeiffer, T. Weitkamp, O. Bunk, and C. David, "Phase retrieval and differential phase-contrast imaging with low-brilliance X-ray sources," *Nature Physics* **2**, p. 258, 2006.

7. F. Pfeiffer, C. Kottler, O. Bunk, and C. David, "Hard X-ray phase tomography with low-brilliance sources," *Physical Review Letters* **98**, p. 108105, 2007.

8. T. Weitkamp, A. Diaz, C. David, F. Pfeiffer, M. Stampanoni, P. Cloetens, and E. Ziegler, "X-ray phase imaging with a grating interferometer," *Optics Express* **12**, pp. 6296–6304, 2005.

9. T. Weitkamp, C. David, C. Kottler, O. Bunk, and F. Pfeiffer, "Tomography with grating interferometers at low-brilliance sources," *Proceedings of SPIE* **6318**, p. 63180S, 2006.

10. F. Beckmann, T. Lippmann, J. Metge, T. Dose, T. Donath, M. Tischer, K. D. Liss, and A. Schreyer, "HARWI-II, the new high-energy beamline for materials science at HASYLAB/DESY," in *Synchrotron Radiation Instrumentation: Eighth International Conference, edited by T. Warwick et al.*, 2004.

11. F. Beckmann, T. Dose, T. Lippmann, R. V. Martins, and A. Schreyer, "The new materials science beamline HARWI-II at DESY," in *AIP Conference Proceedings, SRI 2006*, 2007.

12. W. Reimers, A. R. Pyzalla, A. Schreyer, and H. Clemens, eds., *Neutrons and Synchrotron Radiation in Engineering Materials Science*, Wiley-VCH, 2008.

13. G. Illing, J. Heuer, B. Reime, M. Lohmann, R. Menk, L. Schildwächter, W.-R. Dix, and W. Graeff, "Double beam bent Laue monochromator for coronary angiography," *Rev. Sci. Instrum.* **66(2)**, pp. 1379–1381, 1995.

14. M. Lohmann, W.-R. Dix, J. Metge, and B. Reime, "Instrumentation for diffraction enhanced imaging experiments at HASYLAB," *AIP Conf. Proc. SRI 03 San Francisco, California* **705**, p. 392, 2004.

15. F. Beckmann, T. Donath, J. Fischer, T. Dose, T. Lippmann, L. Lottermoser, R. Martins, and A. Schreyer, "New developments for synchrotron-radiation-based microtomography at DESY," in *Proc. of SPIE; Developments in X-Ray Tomography V, edited by Ulrich Bonse, 6318, 631810*, 2006.

16. M. Engelhardt, C. Kottler, O. Bunk, C. David, C. Schroer, J. Baumann, M. Schuster, and F. Pfeiffer, "The fractional Talbot effect in differential x-ray phase-contrast imaging for extended and polychromatic x-ray sources," *Journal of Microscopy* **232 (1)**, pp. 145–157, 2008.

17. C. Grünzweig, *Neutron Grating Interferometry for Imaging Magnetic Structures in Bulk Ferromagnetic Materials.* PhD thesis, Eidgenössischen Technischen Hochschule Zürich, 2009.

18. T. Donath, *Quantitative X-ray Microtomography with Synchrotron Radiation.* PhD thesis, Fachbereich Physik der Universität Hamburg, 2006.

19. C. David, B. Nöhammer, and H. Solak, "Differential x-ray phase contrast imaging using a shearing interferometer," *Applied Physics Letters* **81(17)**, pp. 3287–3289, 2002.

20. F. Pfeiffer, O. Bunk, C. Kottler, and C. David, "Tomographic reconstruction of three-dimensional objects from hard X-ray differential phase contrast projection images," *Nuclear Instruments and Methods in Physics Research* **A 580**, pp. 925–928, 2007.

21. F. Pfeiffer, M. Bech, O. Bunk, P. Kraft, E. F. Eikenberry, C. Brönnimann, C. Grünzweig, and C. David, "Hard-X-ray dark-field imaging using a grating interferometer," *Nature Materials* **7**, pp. 134–137, 2008.

22. C. David, J. Bruder, T. Rohbeck, C. Grünzweig, C. Kottler, A. Diaz, O. Bunk, and F. Pfeiffer, "Fabrication of diffraction gratings for hard X-ray phase contrast imaging," *Microelectronic Engineering* **84**, p. 11721177, 2007.

23. R. W. Fonda, J. F. Bingert, and K. J. Colligan, "Development of grain structure during friction stir welding," *Scripta Materialia* **51**, pp. 243–248, 2004.

24. J. D. Robson, N. Kamp, and A. Sullivan, "Microstructural modelling for friction stir welding of aluminium alloys," *Materials and Manufacturing Processes* **22**, pp. 450–456, 2007.